A comparison of viscous-plastic sea ice solvers with and without replacement pressure

Madlen Kimmritz[a,*], Martin Losch[b], Sergey Danilov[b,c]

[a] *Nansen Environmental and Remote Sensing Center and Bjerknes Centre for Climate Research, Bergen, Norway*
[b] *Alfred Wegener Institute, Bremerhaven, Germany*
[c] *A. M. Obukhov Institute of Atmospheric Physics RAS, Moscow, Russia*

Abstract

Recent developments of the explicit elastic-viscous-plastic (EVP) solvers call for a new comparison with implicit solvers for the equations of viscous-plastic sea ice dynamics. In Arctic sea ice simulations, the modified and the adaptive EVP solvers, and the implicit Jacobian–free Newton–Krylov (JFNK) solver are compared against each other. The adaptive EVP method shows convergence rates that are generally similar or even better than those of the modified EVP method, but the convergence of the EVP methods is found to depend dramatically on the use of the replacement pressure (RP). Apparently, using the RP can affect the pseudo-elastic waves in the EVP methods by introducing extra non-physical oscillations so that, in the extreme case, convergence to the VP solution can be lost altogether. The JFNK solver also suffers from higher failure rates with RP implying that with RP the momentum equations are stiffer and more difficult to solve. For practical purposes, both EVP methods can be used efficiently with an unexpectedly low number of sub-cycling steps without compromising the solutions. The differences between the RP solutions and the NoRP solutions (when the RP is not being used) can be reduced with lower thresholds of viscous regularization at the cost of increasing stiffness of the equations, and hence the computational costs of solving them.

*Corresponding author
Email addresses: madlen.kimmritz@nersc.no (Madlen Kimmritz), martin.losch@awi.de (Martin Losch), sergey.danilov@awi.de (Sergey Danilov)

Preprint submitted to Ocean Modelling *May 7, 2017*

Keywords: Sea ice, VP rheology, EVP rheology, MITgcm, adaptive relaxation parameter, JFNK, replacement pressure
2010 MSC: 00-01, 99-00

1. Introduction

Sea ice covers only approximately 7% of the global ocean, but it is an important contributor to the surface heat budget and hence an important player for the Earth's climate. It undergoes strong annual variations and it is affected by climate change about twice as much as globally averaged quantities (Vancoppenolle, 2008). Thus, for any application in climate sciences, it is important to describe the physics of sea ice accurately. Dynamic and thermodynamic processes determine sea ice evolution. While thermodynamic processes lead to melting and growth of the ice, sea ice dynamics describe the motion and deformation of the sea ice pack under the action of wind forces, ocean currents and internal ice stresses. We focus on the dynamics of sea ice. Most state-of-the-art numerical sea ice model dynamics are based on a quasi-continuum assumption and treat sea ice as a non-Newtonian fluid with an appropriate formulation of rheology.

The dynamical nature of sea ice is strongly non-linear (Hibler, 1988), mainly due to the strong non-linearity of the internal ice stresses, and encompasses a wide variety of ice types and features. Thus, any realistic rheology for sea ice, that is the relationship between the internal ice stresses and the ice strain rates, leads to a very stiff system of non-linear equations and requires efficient solution methods with good numerical convergence properties.

In spite of recent developments, such as the elastic-plastic-anisotropic (Tsamados et al., 2013) or the elasto-brittle rheology (Girard et al., 2011, Bouillon and Rampal, 2015), the vast majority of sea ice models are based on the viscous-plastic (VP) rheology (Hibler, 1979). To our knowledge, an implicit Jacobian-free Newton-Krylov (JFNK) solver (Lemieux et al., 2010, 2012, Losch et al., 2014) is one of the most efficient way to obtain accurate (machine precision) solutions available today for the highly non-linear VP model, but such a solver is still computationally very expensive. In this manuscript we use converged JFNK solutions as a reference.

An alternative is to use fully explicit Elastic-Viscous-Plastic (EVP) schemes in which an elasticity term has been added to the stress equation in order to relax the restrictive time step limitation of VP-models. In this case, sub-cycling within each external time level is applied in order to damp out the artificial elastic waves. The idea (Hunke and Dukowicz, 1997, Hunke, 2001) is now widely used in numerical sea ice modeling. Losch et al. (2010), Losch and Danilov (2012) and Lemieux et al. (2012) showed that the original attempt does not converge to the VP solution, and instead produces different deformation fields, weaker ice and smaller viscosities. To overcome this issue, Lemieux et al. (2012) added an inertial term in the momentum equations. Bouillon et al. (2013) reformulated this modified EVP (mEVP) scheme as a pseudo-time iterative process, which by construction should converge to the VP solution. Kimmritz et al. (2015) formulated a criterion that ensured (linear) convergence of the scheme proposed in Bouillon et al. (2013) in a set of experiments with simple geometry and forcing.

In the mEVP method, two constant sub-cycling parameters α and β determine the convergence rates of the ice stress and momentum equations to the VP solution in the pseudo-time iteration. They need to be sufficiently large, typically order of several hundreds, to ensure stability of the scheme. Large sub-cycling parameters, however, also mean slower convergence rates and thus likely require a larger number of sub-cycling steps N_{EVP} to reach a reasonable degree of convergence. Full convergence (i.e. the residuals of the momentum and stress equations are reduced to machine precision) requires many thousand sub-cycles and has been found to be too expensive to be practical (Kimmritz et al., 2015).

Kimmritz et al. (2016) modified mEVP further and determined the sub-cycling parameters locally according to local stability requirements to ensure sufficient accuracy of the sub-cycling. In this adaptive EVP (aEVP) scheme, the sub-cycling parameters vary in space and time, while the number of sub-cycling steps is kept constant as in the mEVP scheme. The aEVP scheme requires large values for the sub-cycling parameters α and β only in a few areas where the ice is strong and immobile (Kimmritz et al., 2016). If one accepts poor reduction of residuals in these areas (i.e. low convergence), a smaller overall number of sub-cycling steps can be used without compromising accuracy almost everywhere compared to mEVP.

A practical performance analysis of aEVP and mEVP with realistic ocean geometries and forcing was not a subject of Kimmritz et al. (2016) and is done here. We will show that for both explicit schemes we can reproduce solutions that are nearly indistinguishable (see below) from reference solutions obtained with the converged JFNK solver. Tightly connected to the choice of solution techniques is the practical question of selecting the number of sub-cycling steps N_{EVP}. Because running the mEVP and aEVP schemes to full convergence is computationally very expensive, these schemes, in practice, will be run with incomplete convergence. We show that, in order to save computer time, N_{EVP} can be reduced well below the value required by formal theoretical consideration with only very limited effect on the obtained solutions.

Another, almost accidental, result emerges that, in contrast to the simple test cases in Kimmritz et al. (2016), the convergence of the mEVP and aEVP schemes to the VP solution and the performance of the JFNK solver in realistic configurations are sensitive to the regularization of the internal ice strength in the viscous regime. Hibler (1979) limited large viscosities for very small strain rates in the internal stress equations by maximal values thereby introducing viscous behavior to the model. Bounding the viscosities from above is almost equivalent to limiting the strain rate parameter Δ from below. In some models (including ours), this regularization is implemented by adding a minimum Δ_{min} to Δ (see Section 2 for more details) to yield a smooth regularization (Kreyscher et al., 2000). Lemieux et al. (2010) implemented a narrower but still smooth transition from the plastic to the viscous regime by regularizing the viscosities with a hyperbolic tangent (tanh) function. With regularized viscosities, ice strength gradients (i.e., ice thickness and concentration gradients) lead to creep of ice in the absence of forcing. Modifying the compressive strength in analogy to the regularized viscosities removes this spurious effect (Hibler and Ip, 1995). The physical effect of this so-called replacement pressure (RP) on large scale simulations was compared to other rheologies (Geiger et al., 1998), and most, if not all, sea ice models use RP to avoid spurious motion. We re-evaluate the effects of the replacement pressure in the context of numerical convergence of the mEVP and aEVP schemes.

This article is structured as follows. Section 2 describes the sea ice momentum equations followed by a brief introduction of solution methods in Section 3. Section 4 presents the numerical results. A discussion of the results and the conclusions are given in Sections 5 and 6.

2. Description of model sea ice dynamics

The dynamics of sea ice is governed by the sea ice momentum balance

$$m(\partial_t + f\mathbf{k}\times)\mathbf{u} = \boldsymbol{\tau}_a + \boldsymbol{\tau}_o - mg\nabla H + \mathbf{F}, \tag{1}$$

where m is the ice (plus snow) mass per unit area, f is the Coriolis parameter, $\mathbf{k}$ the vertical unit vector, $\mathbf{u}$ the ice velocity, $\boldsymbol{\tau}_a$ and $\boldsymbol{\tau}_o$ the wind and ocean stresses, g the acceleration due to gravity, H the sea ice surface elevation, and $\mathbf{F} = \nabla\cdot\boldsymbol{\sigma}$ the divergence of internal stresses in sea ice. In our implementation, $\boldsymbol{\tau}_a$ is independent of the ice velocities. The ocean stress is prescribed by $\boldsymbol{\tau}_o = -C_d\rho_o(\mathbf{u}-\mathbf{u}_o)|\mathbf{u}-\mathbf{u}_o|$ with ocean–ice drag C_d, ocean water density ρ_o and ocean velocity $\mathbf{u}_o$.

The viscous plastic constitutive law is given by

$$\sigma_{ij}(\mathbf{u}) = 2\eta\dot{\epsilon}_{ij} + \left[(\zeta-\eta)\dot{\epsilon}_{kk} - \frac{P}{2}\right]\delta_{ij} \tag{2}$$

with the strain rates

$$\dot{\epsilon}_{ij} = \frac{1}{2}\left(\partial_i u_j + \partial_j u_i\right) \tag{3}$$

where the indices i and j denote the x and y directions. The ice strength P is parameterized as $P = P^*\, h\, a\, e^{-c^*(1-a)}$, where a is the ice concentration (or ice compactness) and h is the mean thickness of the grid cell; the constants P^* and c^* are set to 27500 Nm^{-2} and 20 (Lemieux et al., 2010). The bulk and shear viscosities are given by $\zeta = P/(2\Delta)$ and $\eta = \zeta/e^2$, such that the stress states lie on an elliptic yield curve with the ratio of the semi-major and the semi-minor axis $e = 2$. The parameter Δ is defined as $\Delta = (\dot{\varepsilon}_d^2 + e^{-2}\dot{\varepsilon}_s^2)^{1/2}$ with divergence $\dot{\varepsilon}_d = \dot{\varepsilon}_{11} + \dot{\varepsilon}_{22}$ and shear $\dot{\varepsilon}_s = ((\dot{\varepsilon}_{11} - \dot{\varepsilon}_{22})^2 + 4\dot{\varepsilon}_{12}^2)^{1/2}$.

Thus, the ice is presumed to act as a plastic material, unless the shear and the divergence are very small. If the deformation parameter Δ is below a given threshold ($\Delta < \Delta_{min}$), the ice is treated as a linear-viscous fluid. We implement this by replacing Δ with $\Delta_{reg} = \Delta + \Delta_{min}$ in the definition of ζ and η.

In the case of small strain rates and non-uniform P, changes in the internal ice stress P introduce a slow creep towards equilibrium even if no external forces are being imposed. Hibler and Ip (1995) introduced the so called replacement pressure (RP) $P_r = 2\Delta\zeta = P\Delta/(\Delta + \Delta_{\min})$ to remove this unphysical effect of unforced spontaneous viscous creep. The constitutive law then reads

$$\sigma_{ij}(\mathbf{u}) = 2\eta\dot{\epsilon}_{ij} + \left[(\zeta - \eta)\dot{\epsilon}_{kk}\delta_{ij} - \frac{P_r}{2}\right]\delta_{ij}\,. \tag{4}$$

Note, that P_r is smaller than P in the viscous regime as the strain rates, and hence Δ, tend to zero.

RP is used in virtually all VP models. But because the RP can become small in immobile pack ice, this parameterization may also lead to too low resistance against compression. This can occur for instance when pack ice is pushed against a boundary and then piles up infinitely. Further, we will show that with RP extra pseudo-elastic waves are generated in the EVP case by the pressure gradients that lead to additional instabilities. We denote the formulation which uses equation (4) as RP, and the set of equations which use equation (2) as NoRP. It should be stressed that the RP and NoRP cases are only different when Δ is small (order $\Delta_{\min}$ or less), that is, in the viscous regime. The difference is therefore related to the regularization and depends on the magnitude of $\Delta_{\min}$.

3. Numerical schemes

Both EVP schemes and the JFNK scheme use the same temporal discretisation. Let Δt be the time step length and n the index of the time level. Ice velocities at time level n are computed from the ice concentration, ice and snow thicknesses, the ocean velocity and elevation at time level $n-1$ using an implicit Euler scheme. Dropping the time index for all but the ice velocity, we write:

$$\begin{aligned} m(\mathbf{u}^n - \mathbf{u}^{n-1})\Delta t^{-1} = & - mf\mathbf{k} \times \mathbf{u}^n - C_d \rho_o (\mathbf{u}^n - \mathbf{u}_o)|\mathbf{u}^n - \mathbf{u}_o| \\ & + \mathbf{R} + \nabla \cdot \boldsymbol{\sigma}(\mathbf{u}^n) \end{aligned} \tag{5}$$

where $\mathbf{R}$ includes the ice-air drag and the sea surface tilt. The stress tensor $\boldsymbol{\sigma}(\mathbf{u}^n)$ for NoRP or RP is given by (2) or (4). The momentum equations are discretized in space on a C grid (Losch et al., 2010).

3.1. JFNK solver

After spatial discretization, the N components of the discrete u- and v-velocities can be stacked into an N-dimensional vector $\mathbf{u}$, and the nonlinear equation (5) can be written in vector-matrix form as

$$\mathbf{A}(\mathbf{u}^n)\mathbf{u}^n = \mathbf{b}(\mathbf{u}^n), \tag{6}$$

where $\mathbf{A}$ is an $N \times N$ matrix and $\mathbf{b}$ an N-dimensional vector. In order to find an approximate solution $\mathbf{u}^*$ to this equation within a given tolerance, the JFNK solver uses a Newton method to determine the minimum of the norm of the residual $\mathbf{F} = \mathbf{A}(\mathbf{u})\mathbf{u} - \mathbf{b}(\mathbf{u})$. The linearized Newton problem is solved with a Krylov method (here the Flexible Generalized Minimum RESidual method (FGMRES, Saad, 1993) with right-hand side preconditioning). Further details of the JFNK solver, in particular the preconditioner for the FGMRES method, can be found in Lemieux et al. (2012), Losch et al. (2014).

3.2. EVP schemes

The modified EVP scheme can be thought of as an iterative explicit scheme solving (5) through sub-cycling (Lemieux et al., 2012, Bouillon et al., 2013).

The p-th level of the sub-cycling in the mEVP scheme to determine the solution $\mathbf{u}^n$ from time level $n-1$ reads

$$\boldsymbol{\sigma}_{p+1} - \boldsymbol{\sigma}_p = \alpha^{-1}\Big(\boldsymbol{\sigma}(\mathbf{u}_p) - \boldsymbol{\sigma}_p\Big), \tag{7}$$

$$\mathbf{u}_{p+1} - \mathbf{u}_p = \beta^{-1}\Big(\frac{\Delta t}{m}\nabla\cdot\boldsymbol{\sigma}_{p+1} + \frac{\Delta t}{m}\mathbf{R}_{p+1/2} + \mathbf{u}^{n-1} - \mathbf{u}_p\Big). \tag{8}$$

The term $\mathbf{R}_{p+1/2}$ contains the Coriolis forces, the contributions from the wind and ocean stresses and the sea surface tilt. The sea ice - ocean drag is linearized as $C_d\rho_o|\mathbf{u}_o - \mathbf{u}_p|(\mathbf{u}_o - \mathbf{u}_{p+1})$. The initial values of the sub-cycling are $(\boldsymbol{\sigma}_0, \mathbf{u}_0) = (\boldsymbol{\sigma}^{n-1}, \mathbf{u}^{n-1})$. Once converged $((\boldsymbol{\sigma}_{p+1}, \mathbf{u}_{p+1}) \approx (\boldsymbol{\sigma}_p, \mathbf{u}_p))$, the system provides the solution to (5) as $\mathbf{u}^n = \mathbf{u}_{p+1}$. For convergence, the relaxation parameters α and β need to be large enough to make the iterative scheme stable (to be determined experimentally) and the number N_{EVP} of p-iterations, which is constant through the entire domain, should be large compared to α and β.

In the mEVP method, these constraints for α and β are global, and the most critical region sets the constraint for the entire simulation. As will be shown experimentally, $\alpha = \beta = 300$ is large enough for the experiments in this study and we will use these parameter values from now on.

The aEVP scheme (Kimmritz et al., 2016) is a variant of the mEVP scheme. In order to guarantee stability of the iteration, the relaxation parameters α and β are computed to satisfy the local stability criterion

$$\alpha\beta > \gamma = \zeta\frac{(c\,\pi)^2}{A_c}\frac{\Delta t}{m} \tag{9}$$

in each iteration step. The term $(c\,\pi)^2/A_c$ with area A_c of the local grid cell and factor c accounts for the eigenvalues of the Laplacian operator. We use $c = 0.5$. To satisfy the stability criterion (9), we set $\alpha = \beta = (4\gamma)^{1/2}$. α is also limited from below by a value of 50 to control the accuracy of pseudo-time sub-cycling for weak ice. We note that the right-hand-side of (9) depends on known quantities. Thus the use of varying α and β involves negligible additional costs. N_{EVP} is kept constant in the entire integration domain, but may vary as a function of external time steps. Varying N_{EVP} in space would break time synchronism of computations.

N_{EVP} should be much larger than α, for example, a multiple of α, to guarantee sufficient accuracy of the EVP solution. For $\alpha = 300$, this would lead to an expensive sea ice solver. In this work we will explore the impact of lower N_{EVP} on the quality of the EVP solution. This will also include very low values for $N_{\mathrm{EVP}} < 200$, which are way below the suggestion made in Kimmritz et al. (2016).

In practice, the aEVP scheme leads to much lower values of α and β than used in the mEVP scheme in most parts of the domain, allowing faster local convergence. The formal convergence may be lost in a few localized areas with very thick and immobile ice, but since ice velocities will be small in these cases, the errors incurred are expected to be small. Examples are given in the following sections.

3.3. Model setup

Our regional model is based on the MITgcm (Marshall et al., 1997, MITgcm Group, 2016). The domain covers the Arctic, the North Atlantic and the Canadian Arctic Archipelago (CAA). In the Atlantic sector the domain reaches down to 50N in the center and to 45N near the corners of the domain. In the Pacific sector the domain boundaries are located at about 69N (south of the Bering Strait). We use a quarter degree grid with a horizontal grid spacing of about 27 km and 33 vertical levels. The grid is rotated so that the grid equator runs through the North Pole. The same model configuration has been used and described in Castro-Morales et al. (2014). We only repeat relevant details here. The setup is forced with atmospheric fields of the Climate Forecast System Reanalysis (NCEP–CFSR) (Saha et al., 2010). The sea ice model uses simple zero-layer thermodynamics and two thickness categories (thick ice and thin ice including open water as in Hibler, 1979), but provides different VP solvers (Losch et al., 2010, 2014, Kimmritz et al., 2016). The available options are the JFNK solver, the mEVP and aEVP schemes.

We use no-slip/no-flow boundary conditions for the ice drift velocities and no-flux conditions for thickness and concentration at land boundaries. For the open boundaries near 55°N we impose von-Neumann conditions for drift velocities and zero Dirichlet conditions for thickness and concentration; hence P is also zero at open boundaries. The model is run with different solvers for sea ice dynamics (mEVP, aEVP, and JFNK) over an integration period of six years. All experiments are started from a restart file on Jan 01, 1993 after a 35-year spinup run with the JFNK solver using RP.

4. Results

4.1. Performance of the explicit schemes

Reaching full convergence of the mEVP and aEVP schemes is too expensive for all practical purposes (see Kimmritz et al., 2015, 2016). We run simulations using both mEVP and aEVP and a range of values of sub-cycling time steps that are numerically affordable ($N_{\text{EVP}} = 500, 300, 200, 100, 50.$). We do this in order to explore the consequences of incomplete convergence at each external (advective) time level.

The schemes use the NoRP method (we will examine the differences between the NoRP and RP cases in the next section). For the regularization of the internal ice stresses we use $\Delta_{\min} = 2 \times 10^{-9}\,\text{s}^{-1}$. Figure 1 shows the residual $\beta|\mathbf{u}^{p+1} - \mathbf{u}^{p}|$ of the momentum equation related to the zonal velocity component after one month of integration for the mEVP and the aEVP scheme using $N_{\text{EVP}} = 50$ and 500. The residual characterizes the accuracy of the balance between the terms within the round brackets in (8). For aEVP, the residuals are about one order of magnitude smaller than for mEVP. The mean absolute aEVP residual for $N_{\text{EVP}} = 50$ is similar in magnitue to the mean absolute mEVP residual for N_{EVP} between 200 and 300.

The smaller residuals of the aEVP scheme, according to equation (9), are due to the much lower values of α and β (and thus faster local convergence) in most areas of the ice covered region. We illustrate this in Fig. 2(a – b) with two spatial maps showing the field of α for the month of March and September 1993; other years are similar as the timeseries in Fig. 2(c) indicates. The spatial distribution of α shows little sensitivity to N_{EVP} in the range of 50 to 500. Note that no upper bound on α is imposed.

In winter conditions, the constraint (9) requires high values for α of about 300 in some areas (i.e., the CAA and sporadically other coasts) and also locally in the central Arctic. Elsewhere, the values of α are about 100 or less (remember that α is limited from below by a value of 50 to control the accuracy of pseudo-time sub-cycling for weak ice).

The CAA is characterized by land-fast ice in straits (Howell et al., 2016), multi year ice, with fewer keels and ridging, and high summer ice concentrations (Melling, 2002). Although these details are not parametrized nor resolved in our model, the simulated winter sea ice in the CAA is also rather compact, immobile and characterized by small values of Δ.

As a consequence, the stability parameter α selected by the aEVP scheme is large in the CAA in winter (see Fig. 2), which results in similar residual errors as shown by the mEVP scheme. For $N_{\mathrm{EVP}} = 50$, shown in Fig. 1(a – b), the mEVP and aEVP schemes are far from converged. The residual errors in the CAA prove to be smaller than in the open ocean because the ice velocities in the CAA are small. For $N_{\mathrm{EVP}} = 500$ (Fig. 1(c – d)), the aEVP scheme demonstrates better convergence in the open ocean, and the situation reverses.

In summer conditions, α drops to its lower bound over most of the ice covered areas, including the CAA. The small values of α in most of the domain also explain why one may hope to reach a reasonable behavior of the aEVP scheme with relatively low N_{EVP}. As the maximum values of α obtained for the aEVP scheme (Fig. 2(c)) are of about 300, using the values $\alpha = \beta = 300$ for the mEVP scheme is sufficient to maintain stability and results in optimal convergence rates.

Now we compare the solutions obtained with mEVP and aEVP with moderate N_{EVP} to a reference obtained with the converged JFNK solver in order to assess the quality of the incompletely converged EVP solutions. Therefore we use two metrics: In order to indicate the errors in the mass field, which stem from the inaccuracies in the velocity field, we consider monthly mean values of the ice thickness field. To evaluate the error in the ice solver for the highly non-linear ice dynamics, we analyse the states of Δ on particular time levels. This field reflects the errors in both divergence and shear. Furthermore, it also indicates where the viscous regularization takes place. Figure 3 shows the solutions (panels (a) – (d) for $N_{\mathrm{EVP}} = 50$ and panels (e) – (h) for $N_{\mathrm{EVP}} = 200$) for March 1997 when differences with respect to the JFNK solution have already accumulated over about five years of integration. Although the differences in thickness (left column) are larger for lower N_{EVP}, they are small compared to both the magnitude of thickness in the reference solution and the uncertainties in satellite observations of sea ice thickness. The latter depend on the type of observational data and may easily reach tens of centimeters (Zygmuntowska et al., 2014, Kwok and Rothrock, 2009). For more information, see also e.g. Alexandrov et al. (2010), Kaleschke et al. (2012). The same is true for the ice concentration fields (not shown).

Further, mEVP and aEVP give similar results. As expected, the differences to the JFNK solution are higher for mEVP. Note, for example, the better agreement between aEVP and the reference for Δ in the Kara Sea. Although initially (in the first winter season) the aEVP shows smaller errors, the summer season, when the contribution from rheology is less important, makes the error comparable and they remain so for the rest of the simulation. The colorbar in Figure 3 hides anomalously high differences that can be found sporadically over very localized areas in the marginal ice zone and at points adjacent to the coast. In Table 1 we present the errors for the Central Arctic ($a_{ice} > 0.8$) and for the marginal ice zones ($a_{ice} < 0.8$) for March 1997 separately. The errors are larger in the marginal ice zones, especially for the Δ field. They are partly linked to larger ice velocities, so that the advection of accumulated errors become more important. Except for the ice margin, the errors of both schemes drop down when the number of sub-cycles is increased, with errors staying smaller for aEVP. In the interior Arctic, the mean absolute differences between solutions remain small for the entire integration. For ice thickness, they are generally smaller than 1 cm, for concentration below 0.5% points, and for ice drift below

	N_{EVP}	$a_{ice} < 0.8$ mEVP	aEVP	$a_{ice} > 0.8$ mEVP	aEVP
$\|\|h - h_{\mathrm{ref}}\|\|$	50	7.3	7.4	1.1	0.92
	200	7.3	5.2	0.99	0.76
$\|\|\Delta - \Delta_{\mathrm{ref}}\|\|$	50	4.2×10^{-7}	3.9×10^{-7}	2.6×10^{-8}	1.6×10^{-8}
	200	3.5×10^{-7}	3.5×10^{-7}	1.7×10^{-8}	1.3×10^{-8}

Table 1: Mean absolute differences for March 1997 in the ice thickness (in cm) and in the Δ field (in s^{-1}) between the reference solution and the mEVP and the aEVP scheme for different choices of N_{EVP} in areas with different ice concentrations.

	N_{EVP}	$a_{ice} < 0.8$ mEVP	aEVP	$a_{ice} > 0.8$ mEVP	aEVP
$\|\|h - h_{\mathrm{ref}}\|\|$	50	0.41	0.31	1.4	0.69
	200	0.95	0.87	0.72	0.54
$\|\|\Delta - \Delta_{\mathrm{ref}}\|\|$	50	1.3×10^{-7}	1.3×10^{-7}	1.4×10^{-8}	1.2×10^{-9}
	200	1.2×10^{-7}	1.2×10^{-7}	9.1×10^{-9}	8.0×10^{-9}
$\|\|a_{ice} - a_{ice,\mathrm{ref}}\|\|$	50	0.84	0.64	0.50	0.34
	200	1.6	1.4	0.27	0.23
$\|\|u - u_{\mathrm{ref}}\|\|$	50	0.76	0.79	8.8×10^{-2}	6.8×10^{-2}
	200	0.65	0.66	5.2×10^{-2}	4.5×10^{-2}
$\|\|v - v_{\mathrm{ref}}\|\|$	50	0.94	0.91	8.4×10^{-2}	6.2×10^{-2}
	200	0.74	0.72	4.4×10^{-2}	3.8×10^{-2}

Table 2: Mean absolute differences as average over the entire period in the ice thickness (in cm), in the Δ field (in s^{-1}), in the ice concentration (in %), and in the horizontal velocities u and v (in cm s^{-1}) between the reference solution and the mEVP and the aEVP scheme for different choices of N_{EVP} in areas with different ice concentrations.

$1\,\mathrm{mm\,s^{-1}}$ (Table 2). The differences are up to one order magnitude larger in the marginal ice zone; except for ice thickness, because the ice is generally thinner in these regions than in the Central Arctic.

The aEVP scheme allows smaller values of α over large parts of the Arctic which improves the convergence locally. In contrast, the mEVP scheme uses large α everywhere, which slows down the convergence in the regions where stability constraints do not require α to be large.

Figure 4 depicts the timeseries of the absolute differences of the mean ice thickness between the JFNK solution and the EVP solutions for the entire period of integration. It shows that the differences for the aEVP and mEVP schemes accumulate with time, with stronger accumulation rate for smaller N_{EVP} (compare panels (a) and (b)). During the first year of integration the mEVP solutions tend to be more sensitive to the choice of N_{EVP} than the aEVP solutions. Initially the aEVP scheme simulates smaller errors, but with time, the accumulated model errors make the differences of mEVP and aEVP similar to each other. The runs with smaller N_{EVP} show larger deviations from the reference solution. But even for $N_{\mathrm{EVP}} = 50$, the aEVP and the mEVP solutions are of comparable accuracy. For larger values of $\alpha = \beta = 500$, the mEVP solution shows larger deviations from the reference solution when N_{EVP} becomes smaller, because with large α and β the convergence rates are low (not shown).

Note that within the first year of integration the largest increase in the error for the aEVP scheme takes place in summer when the internal ice stresses are least important. It is thus likely that small errors in the velocity field are amplified by chaotic advection in summer, when the rheology only plays a minor role and the impact of oceanic and atmospheric surface stress terms on the momentum balance is increased. The results for the ice concentration and the Δ fields are similar (not shown).

In summary, for the given setup the partial convergence of mEVP and aEVP (the use of small values for N_{EVP}) does not lead to significant errors (relative to the JFNK solutions), as long as the stability of the iterative process is maintained. The overall deviations from the reference solution are small and tend to be less for aEVP but both solvers show more similarity than differences. That is, the development of the mean absolute deviation from the reference solution shows the same trend for aEVP and mEVP after the first winter season with aEVP being slightly closer to the reference solution. The spatial distribution of the ice concentration, ice thickness and the Δ-field agree in structure and magnitude with improved agreement for larger N_{EVP}.

4.2. The impact of the pressure replacement method

The pressure replacement method (Hibler and Ip, 1995) prevents sea ice from viscous creep in the absence of external forcing. Here, we are interested in the impact of RP and NoRP on the ice state and the convergence of the JFNK, mEVP and aEVP schemes. The following results are obtained with the JFNK solver that we call converged when the residual has been reduced by a factor of 10^{-4}. A failure of a Newton iteration is registered, when the residual is not reduced by this factor within 100 Newton iterations; a maximum number of 50 Krylov steps per Newton step is used (see Lemieux et al., 2012, Losch et al., 2014, for details). We start with the examination of the ice state simulated with and without RP. Numerical aspects will be considered afterwards.

4.2.1. Impact on the ice state

Figure 5 illustrates the differences between the NoRP and the RP solutions by the example of mean 1997-March values of ice thicknesses (panels (a) – (f)) and Δ fields (panels (g) – (l)). In this figure we focus on the northern CAA and the Lincoln Sea, as the impact of RP is most prominent in that area. We start with the case $\Delta_{\mathrm{min}} = 2 \cdot 10^{-9}\mathrm{s}^{-1}$ (Hibler and Ip, 1995) (Fig. 5(a – c) and Fig. 5(g – i)).

In winter, very thick ice of locally up to 12 m is formed in the Lincoln Sea for RP. In contrast, for NoRP, the ice is thinner by $0.2 - 0.4$ m in a large region extending from the northern part of the Nares Strait (Robeson Channel) into the Lincoln Sea, and largest local values drop to about 9m (while not necessarily realistic, such local values are commonly simulated by sea ice models of the type used here). This is so because, in contrast to the RP simulation, in the NoRP simulation immobile ice with differing ice thicknesses undergoes (slow) creep. Thus, there is more ice transport through the Nares Strait (compare eqs. (2) and (4) in the viscous regime, $\Delta \ll \Delta_{\min}$, in the presence of ice thickness gradients), so that a trough of thinner ice extends from the Robeson Channel into the Lincoln Sea. This trough forms already in the first year of the model run (not shown) and persists throughout the entire simulation. Differences between RP and NoRP in Δ (Fig. 5(g – i)) are from about 1% to 10%, both in the interior and in the weaker ice zones. In analogy with the ice thickness fields, the values for Δ in the Nares Strait are lower for RP than for NoRP. Furthermore, for RP values of Δ lower than $10^{-9}\,\mathrm{s}^{-1}$ (viscous regime) are only found in the CAA. For NoRP such low values are also found at the northern boundary of the CAA, which agrees with the thinner ice simulated there.

The viscous regime represents a regularization so that smaller values of the regularization parameter $\Delta_{\min}$ should lead to smaller differences between the two cases. This is seen in Fig. 5(d – f) – and Fig. 5(j – l), where we used $\Delta_{\min} = 2 \cdot 10^{-11}\,\mathrm{s}^{-1}$ (two orders of magnitude smaller than before). The maximum thicknesses for this choice of $\Delta_{\min}$ are 12 m and 10.7 m for RP and NoRP. These values are closer to each other and closer to the RP case with larger $\Delta_{\min} = 2 \cdot 10^{-9}\,\mathrm{s}^{-1}$. There is no trough in the Robeson Channel in the NoRP case. Compared to the larger $\Delta_{\min}$-case, the differences in the Δ fields are now about one to two orders of magnitudes smaller in regions where Δ is small. The viscous regularization is active at fewer times and only in very small areas; the system remains in a plastic state for a wider range of Δ values.

Polynyas in the Nares Strait can be found in satellite images (e.g. Adams, 2012). These polynyas or regions of thin ice can reach the northern entrance of the strait and even protrude as a tongue into the Lincoln Sea (Allison, 2013). In some winters, a stable ice bridge forms at this entrance to the CAA and blocks any transport into the Nares Strait (Allison, 2013). This situation is similar in the ICESat-derived ice thickness estimates (Maslanik et al., 2007, their Fig. 3d): As in our RP simulations stronger ice is formed in the Lincoln Sea instead of

	RP09	NoRP09	RP11	NoRP11
# Krylov steps	$1.10 \cdot 10^7$	$6.32 \cdot 10^6$	$1.76 \cdot 10^7$	$1.53 \cdot 10^7$
# Newton steps	$1.26 \cdot 10^6$	$9.96 \cdot 10^5$	$2.35 \cdot 10^6$	$2.05 \cdot 10^6$
# Newton failures	52	5	243	109

Table 3: Accumulated numbers of Krylov and Newton steps and number of failures for RP and NoRP cases using $\Delta_{\min} = 2 \cdot 10^{-9}\,\mathrm{s}^{-1}$ (center block) and $\Delta_{\min} = 2 \cdot 10^{-11}\,\mathrm{s}^{-1}$ (right block) for the years 1993 – 1997.

a trough. Allison (2013) also reports cases where this bridge did not form and ice was transported southwards through the strait. Furthermore, the ICESat data for sea ice thickness in spring (Kwok and Cunningham, 2008, their Fig. 11) do not rule out a trough extending into the Lincoln Sea similar to our NoRP solutions, although in our simulation this trough is much larger.

4.2.2. Numerical aspects

In this section we discuss the numerical properties of the schemes. Although the detected issues might not affect the quality of the solutions for the coarse resolution simulations (here, approximately 27 km grid spacing), they may become more important in simulations on finer meshes (5 km grid spacing or smaller). On finer meshes more dynamical features of the ice are expected to be resolved with larger gradients in the solutions. This may impose new requirements on the convergences of the solvers.

We start with the implicit JFNK solver. Table 3 lists the numbers of Krylov and Newton steps and failures accumulated over the entire integration period. For $\Delta_{\min} = 2 \cdot 10^{-9}\,\mathrm{s}^{-1}$ the RP case requires almost twice as many Krylov steps and about one third more Newton steps than the NoRP case, and the numbers of failures of a Newton iteration is much larger in the RP compared to the NoRP case (note that 243 failures in 6 years of integration with timestep length of 20 minutes is a failure rate of 1.5‰). A hundred times smaller $\Delta_{\min} = 2 \cdot 10^{-11}\,\mathrm{s}^{-1}$ doubles the number of solver steps and strongly increases the number of failures. The increase for RP is not as large as for NoRP, but the scheme still remains more expensive with RP and the number of failures is still larger than in the NoRP case.

For the explicit EVP schemes (where we use a fixed number of sub-cycling steps) the effect of the RP on the convergence is not less dramatic. Both the mEVP and aEVP schemes converge to machine precision after 60000 sub-cycling steps only with NoRP (Fig. 6). The corresponding patterns of the residuals for the u component of the momentum balance are depicted in Figure 7. The residuals in the NoRP case are grid scale noise on the order of machine precision, but for RP the regions with very low values of $\Delta \ll \Delta_{\min}$ (compare with Figure 5) appear to act as the sources of propagating pseudo-elastic waves. These waves, which, by construction, do not appear in the VP solver, are supported because sea ice in the viscous regime is also compressible (Hunke and Dukowicz, 1997). Potentially they lead to grid scale noise. The fact that they are coming from the regions with very small Δ point to the involvement of RP in the source mechanism.

As the waves in the residual fields are still apparent for very large values of $\alpha = \beta$ up to $5 \cdot 10^4$ (not shown here), we claim that convergence down to machine accuracy of the mEVP and aEVP schemes is generally lost if the replacement pressure is used. A plausible reason for the differing convergence behaviors of NoRP and RP can be seen by considering the stress contribution in the momentum in the case when $\Delta \ll \Delta_{\min}$. In the RP case, the ice strength is multiplied with $\Delta/\Delta_{\min}$ and fluctuates in the process of iterations. It stays constant for NoRP, thus providing balance with external forcing. No persistent elastic waves appear in the NoRP scheme which supports this attempt of a qualitative explanation.

The formal loss of convergence, however, does not necessarily imply that the solutions are compromised. The residual reduction in the first 500 sub-cycling steps is of the same order in both the RP and NoRP cases (Figure 6). Thus, the elastic waves in both schemes are likely damped to a comparable extent during the first 500 sub-cycling steps. The choice of $\alpha = \beta = 300$ and $N_{\mathrm{EVP}} = 500$ ensures a convergence towards the VP solution for both the RP and NoRP cases.

Figure 8 shows snapshots of Δ for $\Delta_{\text{min}} = 2 \cdot 10^{-9}\,\text{s}^{-1}$ of the JFNK and the mEVP scheme at the end of the first month. In the CAA and for RP, the mEVP solution shows slightly larger values of Δ than in the reference solution; note that the patterns of Δ for RP and NoRP are very similar over the major part of the domain. Differences occur in regions with low values of Δ. Although the EVP solutions might be close to the JFNK solutions even if their convergence is impaired by using RP, applying an EVP method requires awareness of its potentially critical tendency to have wave signals in the residuals.

If one minimizes the difference between RP and NoRP by choosing smaller values of Δ_{min} larger values of the stability parameters and hence more iterations are necessary. For example, for $\Delta_{\text{min}} = 2 \cdot 10^{-11}\,\text{s}^{-1}$, values of $\alpha = \beta$ should be as large as 3000 to ensure a stable mEVP scheme. Large α and β slow down convergence, so that for values of 3000, 500 sub-cycling steps are not sufficient to get acceptable solutions. Even with $N_{\text{EVP}} = 5000$, Δ is too small in areas of almost immobile ice for both mEVP and aEVP compared to the reference solution (not shown), so that even more—too many—sub-cycling steps are required for acceptable convergence. In summary, too low values of Δ_{min} make the momentum equations harder to solve, so that the EVP schemes become prohibitively expensive and loose their advantages.

5. Discussion

The discussion of the replacement pressure was prompted by the observation that the convergence of mEVP and aEVP solvers is compromised in realistic configurations when the replacement pressure is used. In both cases, the convergence rate for RP is affected by the stronger singularity (non-differentiability) of the internal ice strength term in the viscous regime, that is, by the additional non-linear factor $\Delta/(\Delta + \Delta_{\text{min}})$. With lower values of Δ_{min} the system does not enter the viscous regime as often, so that the RP and NoRP cases are more similar.

The JFNK solver is also sensitive to the use of the replacement pressure, that is, it requires more iterations with replacement pressure than without. The observed increase in the number of iterations with the reduction of $\Delta_{\min}$ is consistent with the general sensitivity of the JFNK solver to details of the regularization (e.g., Lemieux et al., 2010). The notably less efficient convergence in the RP case is a new behavior that has not been reported so far. It is related to the presence of the $\Delta/(\Delta+\Delta_{\min})$ multiplier in the internal ice strength term.

The mEVP and aEVP solvers converge through the propagation of decaying pseudo-elastic waves. For NoRP, the ice strength is constant within one time step, thus providing balance with external forcing in situations when immobile ice is being pushed against the coastline. In the viscous regime when $\Delta \ll \Delta_{\min}$, the RP ice strength is scaled effectively with $\Delta/\Delta_{\mathrm{reg}}$ and hence changes from iteration to iteration, so that no stable balance with the forcing can develop. As a result, the areas in the CAA of very small Δ are sources of wave noise that propagates and occupies a large portion of the ice-covered domain. Any substantial reduction of $\Delta_{\min}$ that would minimize areas of viscous regularization cannot be recommended because it would require larger α, β, and N_{EVP}. We saw that in spite of the formal lack of convergence of the EVP solvers in the RP case the solutions appear useful. This statement may change with higher spatial resolution when linear kinematic features may be (partly) resolved and the ice fields become highly heterogeneous and variable (e.g. Wang and Wang, 2009, Losch et al., 2014, Wang et al., 2016).

The NoRP approach appears to have numerical advantages, but solutions with and without RP are also different. On the one hand, the RP method leads to thicker ice especially in areas where ice "gets stuck" in narrow straits and bays and is already unrealistically thick. This behavior can be explained by the factor $\Delta/(\Delta + \Delta_{\min})$ that tends towards zero in nearly immobile ice with no strain. The RP is then too small to resist further (slow) compression and ice piles up, for example when pushed towards the coast. On the other hand, the unphysical aspect of the NoRP method leads to unforced motion of ice that the RP method was designed to avoid. In addition, in our simulations, the more plausible behavior in onshore wind conditions without replacement pressure, i.e.

larger compressive strength, leads to ice fields sea-ward of the Nares Strait that appear unrealistic.

In our simulations, the NoRP solutions are more sensitive to the value of Δ_{min} than the RP solution. For smaller values of Δ_{min}, the differences between RP and NoRP solutions are smaller (Fig. 5). Further, with $\Delta_{\text{min}} = 2 \cdot 10^{-11}\,\text{s}^{-1}$, both solutions agree with the RP solution with $\Delta_{\text{min}} = 2 \cdot 10^{-9}\,\text{s}^{-1}$, indicating that the RP solutions are preferable. In particular, the spurious ice trough in the Nares Strait in the NoRP solution disappears with smaller Δ_{min}. The sensitivity of the solutions to details of the stress parametrization also raises the question of the general validity of the VP rheology. The replacement pressure is one parameterization among many in a sea ice model. Like any other parameterization it requires careful tuning with the help of observations. Such a multi-dimensional tuning exercise, which would require comprehensive observational data set, inverse methods and data assimilation techniques, is beyond the scope of this manuscript

The very similar performance of mEVP and aEVP and the apparent agreement with the reference with very low N_{EVP} (much lower than suggested by α and β) came as a surprise. Most likely, it can be explained by the relatively smooth ice distributions of our coarse resolution experiments. On finer meshes, the ice thickness and concentration is expected to be permeated by numerous linear kinematic features (leads in the limit of high resolution) (e.g. Wang and Wang, 2009, Losch et al., 2014, Wang et al., 2016). In this case, the sea ice is characterized by larger gradients, making the solution of the momentum equations more difficult to obtain. For the EVP schemes this means that large values of N_{EVP} consistent with α and β may become necessary to reach a sufficient degree of convergence.

The numerical efficiency of the solvers is difficult to compare. Lemieux et al. (2012) report similar computational efficiency of the JFNK and the EVP method, with comparably slow convergence, in their serial computations with grid spacings between 80 km and 10 km. Refining the meshes will require increasing N_{EVP} for the explicit schemes; for the JFNK solver, a higher resolution can lead to more Krylov and Newton iterations. Lemieux et al. (2010) found a higher failure rate of the JFNK solver with higher resolution; their highest resolution is 10 km. We speculate that convergence becomes a technical issue when the grid spacing is fine enough to resolve multiple highly localized deformation zones (leads). In our experience, this starts with a grid spacing of ~ 5 km. In parallel applications, the EVP solvers are expected to scale better than any implicit solver, but even for the JFNK solver, which involves many global communications, good scaling behavior was found for up to 1000 CPUs on a 1680×1536 grid with 4.5 km grid spacing (Losch et al., 2014).

When only low accuracy is sufficient, the mEVP and aEVP solutions obtained with N_{EVP} as low as 50–300 are faster than a converged JFNK solution. However, the convergence of the linear EVP schemes is slow (linear) and the quadratic convergence of the JFNK solver will be required as soon as high numerical accuracy is needed. As the resolution is refined and more local features are resolved, the underlying problem becomes more difficult to solve and the number of iterations required for acceptable convergence of the mEVP and aEVP solvers may increase substantially; likewise, the computational efforts of the JFNK solver will increase. For a grid spacing of 4.5 km, very small time steps on the order of seconds were required to make the JFNK-solver converge (Losch et al., 2014). In exploratory test simulations with this grid, the mEVP solver did not converge for the tested values of α and β. Most likely, much higher values of α and β are required which in turn will require more iteration cycles N_{EVP}. It is even unclear whether or not convergence of any scheme is even possible at very high resolution, so that any definite statements about the relative efficiency of different numerical schemes have to be postponed. In any case, the relative cost of the sea ice component increases together with the required accuracy, that is, the number of sub-cycles for mEVP and aEVP and with iterations in the JFNK solver. In the light of the current practice of just a few non-linear iterations in sub-optimal solvers or non-converging EVP implementations (e.g. Losch and Danilov, 2012), any improvement towards smoother solutions and stable solvers should be seen as a step forward.

6. Conclusions

Both the modified and the adaptive EVP solvers (mEVP, aEVP) can, in realistic simulations of Arctic sea ice at a coarse resolution of 27 km, generate solutions that are close to a converged reference VP solution obtained with a JFNK solver. Both mEVP and aEVP solvers can even be run with N_{EVP} much smaller than formally required for numerical convergence and still arrive at solutions that differ from the reference solution only in details that for most practical applications will go unnoticed. For example, in the interior Arctic, the mean absolute ice thickness differences, where ice concentrations are larger than 80%, are smaller than 1.5 cm; for the ice concentration, they are smaller than 0.5%, and for the velocity they are less than $1\,\mathrm{mm\,s}^{1}$. Only in the dynamic margical ice zone, where temporal variability is high and models can diverge from each other, the mean absolute differences in the ice concentration and in ice velocities reach 1.6% and $1\,\mathrm{cm\,s}^{1}$ on average. We do not expect, that these conclusions can be extrapolated to finer resolution and more variable forcing fields, but in any forced sea-ice ocean only simulations at coarse resolution, the differences between solvers are likely to remain small. In coupled climate simulations with atmospheric feedbacks, however, these differences may grow and become more significant. We also show that in practice the advantage of locally smaller α and β in the aEVP solver does not lead to large improvements in the solution. We give preference to aEVP, because this solver usually reduces the equation residual more than mEVP with the same number of iterations and because the extra computational effort is low.

We found that without replacement pressure (NoRP) all solvers are more stable and converge faster than with replacement pressure (RP). The replacement pressure can be a source of noise in the residuals of the EVP solvers, eventually impeding full convergence. Hence, from the purely numerical point of view, the NoRP scheme with a moderately small value of $\Delta_{\min} = 2 \cdot 10^{-9}\,\mathrm{s}^{-1}$ offers the advantage of faster convergence, but this is not necessarily supported by physical arguments. We refrain from giving any new recommendations about the value of $\Delta_{\min}$ or the use of RP based on physical arguments, but any user of sea ice models should be aware of the parameter choices and their consequences.

Acknowledgments

We thank the reviewers for their helpful remarks on the manuscript.

S. Adams. *Monitoring of thin sea ice within polynyas using MODIS data*. PhD thesis, University of Trier, 2012.

V. Alexandrov, S. Sandven, J. Wahlin, and O. M. Johannessen. The relation between sea ice thickness and freeboard in the Arctic. *The Cryosphere*, 4(3): 373–380, 2010. doi: 10.5194/tc-4-373-2010.

E. E. Allison. The effects of ice arch formation on currents in Nares Strait during the springs of 2008 and 2009. *Physics and Astronomy Honors Projects*, Paper 14., 2013.

S. Bouillon and P. Rampal. Presentation of the dynamical core of neXtSIM, a new sea ice model. *Ocean Modelling*, 91:23–37, 2015. doi: http://dx.doi.org/10.1016/j.ocemod.2015.04.005.

S. Bouillon, T. Fichefet, V. Legat, and G. Madec. The elastic-viscous-plastic method revisited. *Ocean Modelling*, 71:2–12, 2013.

K. Castro-Morales, F. Kauker, M. Losch, S. Hendricks, K. Riemann-Campe, and R. Gerdes. Sensitivity of Simulated Arctic Sea Ice to Realistic Ice Thickness Distributions and Snow Parameterizations. *J. Geophys. Res.*, 119(1):559–571, 2014. ISSN 2169-9291.

C. Geiger, W. D. Hibler, III, and S. F. Ackley. Large-scale sea ice drift and deformation: Comparison between models and observations in the western Weddell Sea during 1992. *J. Geophys. Res.*, 103(C10):21893–21913, 1998.

L. Girard, S. Bouillon, J. Weiss, D. Amitrano, T. Fichefet, and V. Legat. A new modeling framework for sea-ice mechanics based on elasto-brittle rheology. *Annals of Glaciology*, 52(57):123–132, 2011.

W. D. Hibler, III. A Dynamic Thermodynamic Sea Ice Model. *J. Phys. Oceanogr.*, 9:815–846, 1979.

W. D. Hibler, III. *Modelling Sea Ice Thermodynamics and Dynamics in Climate Studies*, pages 509–563. Springer Netherlands, Dordrecht, 1988. doi: 10.1007/978-94-009-3041-4_12.

W. D. Hibler, III and C. F. Ip. The effect of sea ice rheology on Arctic buoy drift. *J. P.Dempsey and Y. D. S.Rajapakse (eds.) ASME AMD*, 207, Ice Mechanics:255–263, 1995.

S. E. L. Howell, F. Laliberté, R. Kwok, C. Derksen, and J. King. Landfast ice thickness in the Canadian Arctic Archipelago from observations and models. *The Cryosphere*, 10(4):1463–1475, 2016. doi: 10.5194/tc-10-1463-2016.

E. C. Hunke. Viscous-plastic sea ice dynamics with the EVP model: Linearization issues. *J. Comp. Phys.*, 170:18–38, 2001.

E. C. Hunke and J. K. Dukowicz. An Elastic-Viscous-Plastic model for sea ice dynamics. *J. Phys. Oceanogr.*, 27:1849–1867, 1997.

L. Kaleschke, X. Tian-Kunze, N. Maa, M. Mkynen, and M. Drusch. Sea ice thickness retrieval from SMOS brightness temperatures during the Arctic freeze-up period. *Geophysical Research Letters*, 39(5), 2012. ISSN 1944-8007. doi: 10.1029/2012GL050916. L05501.

M. Kimmritz, S. Danilov, and M. Losch. On the convergence of the modified elastic-viscous-plastic method for solving the sea ice momentum equation. *J. Comp. Phys.*, 296:90–100, 2015.

M. Kimmritz, S. Danilov, and M. Losch. The adaptive EVP method for solving the sea ice momentum equation. *Ocean Modelling*, 101:59–67, 2016. ISSN 1463-5003. doi: http://dx.doi.org/10.1016/j.ocemod.2016.03.004.

M. Kreyscher, M. Harder, P. Lemke, and G. M. Flato. Results of the Sea Ice Model Intercomparison Project: Evaluation of sea ice rheology schemes for use in climate simulations. *J. Geophys. Res.: Oceans*, 105(C5):11299–11320, 2000. ISSN 2156-2202. doi: 10.1029/1999JC000016.

R. Kwok and G. F. Cunningham. ICESat over Arctic Sea Ice: Estimation of Snow Depth and Ice Thickness. *J. Geophys. Res.*, 113, 2008. doi: 10.1029/2008JC004753.

R. Kwok and D. A. Rothrock. Decline in Arctic sea ice thickness from submarine and ICESat records: 19582008. *Geophys. Res. Lett.*, 36(15), 2009. ISSN 1944-8007. doi: 10.1029/2009GL039035. L15501.

J.-F. Lemieux, B. Tremblay, J. Sedláček, P. Tupper, St. Thomas, D. Huard, and J.-P. Auclair. Improving the numerical convergence of viscous-plastic sea ice models with the Jacobian-free Newton-Krylov method. *J. Comp. Phys.*, 229 (8):2840–2852, 2010. doi: http://dx.doi.org/10.1016/j.jcp.2009.12.011.

J.-F. Lemieux, D. Knoll, B. Tremblay, D.M. Holland, and M. Losch. A comparison of the Jacobian-free Newton-Krylov method and the EVP model for solving the sea ice momentum equation with a viscous-plastic formulation: a serial algorithm study. *J. Comp. Phys.*, 231(17):5926–5944, 2012.

M. Losch and S. Danilov. On solving the momentum equations of dynamic sea ice models with implicit solvers and the elastic-viscous-plastic technique. *Ocean Modelling*, 41:42–52, 2012.

M. Losch, D. Menemenlis, J.-M. Campin, P. Heimbach, and C. Hill. On the formulation of sea-ice models. Part 1: Effects of different solver implementations and parameterizations. *Ocean Modelling*, 3(1–2):129–144, 2010.

M. Losch, A. Fuchs, J.-F. Lemieux, and A. Vanselow. A parallel Jacobian-free Newton-Krylov solver for a coupled sea ice-ocean model. *J. Comp. Phys.*, 257, Part A(0):901–911, 2014.

J. Marshall, A. Adcroft, C. Hill, L. Perelman, and C. Heisey. A Finite-Volume, Incompressible Navier Stokes Model for Studies of the Ocean on Parallel Computers. *J. Geophys. Res.*, 102(C3):5753–5766, 1997.

J. A. Maslanik, C. Fowler, J. Stroeve, S. Drobot, J. Zwally, D. Yi, and W. Emery. A younger, thinner Arctic ice cover: Increased potential for rapid, extensive sea-ice loss. *Geophys. Res. Lett.*, 34(24), 2007. ISSN 1944-8007. doi: 10.1029/2007GL032043. L24501.

H. Melling. Sea ice of the northern Canadian Arctic Archipelago. *J. Geophys. Res.: Oceans*, 107(C11):2–1–2–21, 2002. ISSN 2156-2202. doi: 10.1029/2001JC001102. 3181.

MITgcm Group. MITgcm User Manual. Online documentation, MIT/EAPS, Cambridge, MA 02139, USA, 2016. `http://mitgcm.org/public/r2_manual/latest/online_documents`.

Y. Saad. A Flexible Inner-Outer Preconditioned GMRES Method. *SIAM J. Sci. Comput.*, 14(2):461–469, 1993.

S. Saha, S. Moorthi, H.-L. Pan, X. Wu, J. Wang, S. Nadiga, P. Tripp, R. Kistler, J. Woollen, D. Behringer, H. Liu, D. Stokes, R. Grumbine, G. Gayno, J. Wang, Y.-T. Hou, H.-Y. Chuang, H.-M. H. Juang, J. Sela, M. Iredell, R. Treadon, D. Kleist, P. Van Delst, D. Keyser, J. Derber, M. Ek, J. Meng, H. Wei, R. Yang, S. Lord, H. Van den Dool, A. Kumar, W. Wang, C. Long, M. Chelliah, Y. Xue, B. Huang, J.-K. Schemm, W. Ebisuzaki, R. Lin, P. Xie, M. Chen, S. Zhou, W. Higgins, C.-Z. Zou, Q. Liu, Y. Chen, Y. Han, L. Cucurull, R. W. Reynolds, G. Rutledge, and M. Goldberg. The NCEP Climate Forecast System Reanalysis. *Bull. Amer. Meteor. Soc.*, 91:1015–1057, 2010. doi: 10.1175/2010BAMS3001.1.

M. Tsamados, D. L. Feltham, and A. V. Wilchinsky. Impact of a new anisotropic rheology on simulations of Arctic sea ice. *J. Geophys. Res.: Oceans*, 118(1): 91–107, 2013. doi: 10.1029/2012JC007990.

M. Vancoppenolle. *Modelling the mass balance and salinity of Arctic and Antarctic sea ice.* Presses univ. de Louvain, 2008.

K. Wang and C. Wang. Modeling Linear Kinematic Features in Pack Ice. *J. Geophys. Res.*, 114(C12), 2009. ISSN 2156–2202. doi: 10.1029/2008JC005217.

Q. Wang, S. Danilov, T. Jung, L. Kaleschke, and A. Wernecke. Sea Ice Leads in the Arctic Ocean: Model Assessment, Interannual Variability and Trends. *Geophys. Res. Lett.*, 43:7019–7027, 2016. doi: 10.1002/2016GL068696.

M. Zygmuntowska, P. Rampal, N. Ivanova, and L. H. Smedsrud. Uncertainties in Arctic sea ice thickness and volume: new estimates and implications for trends. *The Cryosphere*, 8(2):705–720, 2014. doi: 10.5194/tc-8-705-2014.

List of Figures

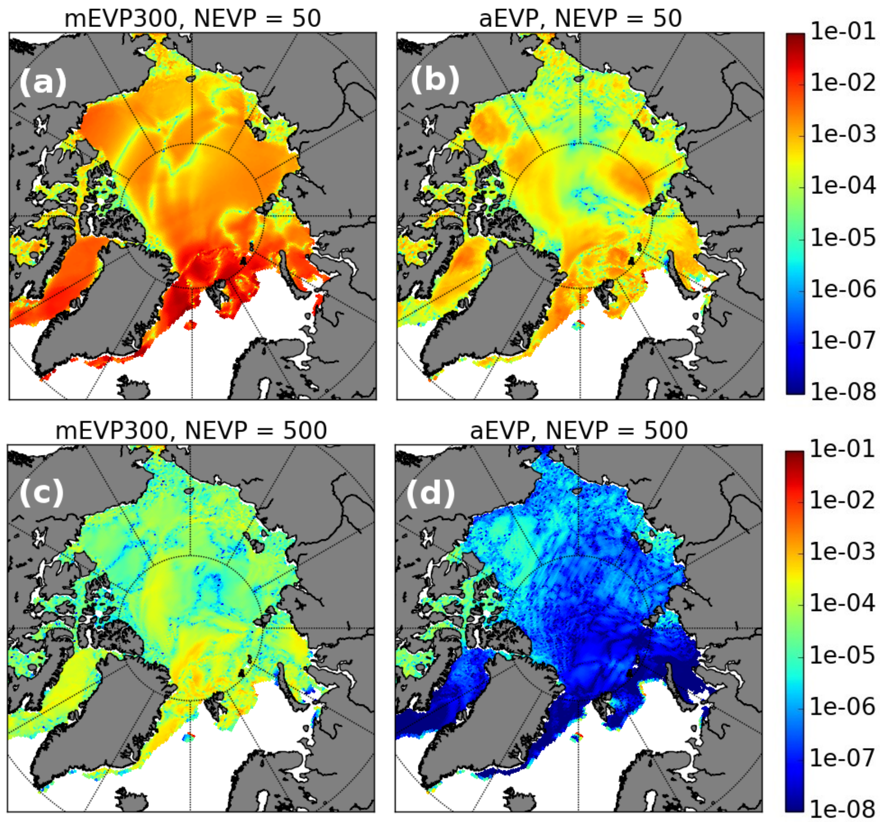

Figure 1: Absolute values of the residuals in the momentum equation for the zonal velocity component (in $\mathrm{m\,s^{-1}}$) after one month of integration at the end of January 1993 for the mEVP (with $\alpha = \beta = 300$) and the aEVP scheme for $N_{\mathrm{EVP}} = 50$ (panels (a) and (b)) and $N_{\mathrm{EVP}} = 500$ (panels (c) and (d)). The residuals have the same units as the velocity.

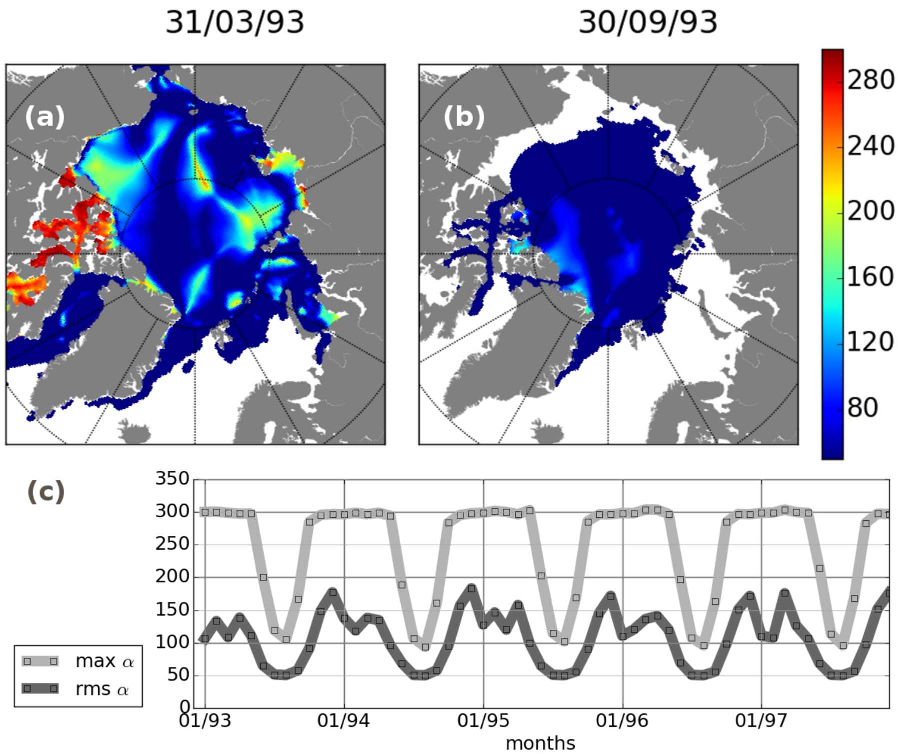

Figure 2: The α field in the aEVP computation with $N_{\mathrm{EVP}} = 500$ at the end of 31/03/93 (panel (a)) and 30/09/93 (panel (b)). Time series of maximal and root mean square values of α at the last sub-cycling in the aEVP scheme of each month (panel (c)).

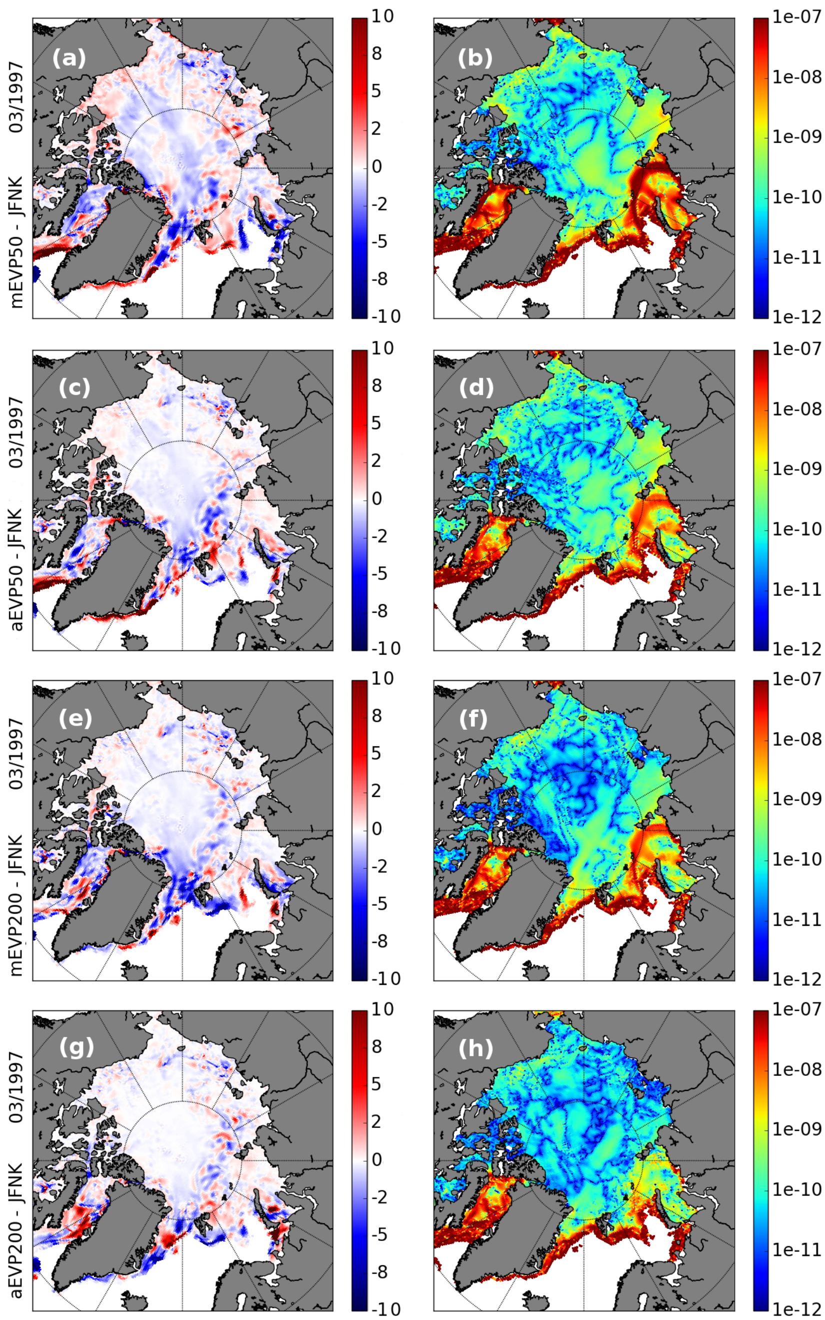

Figure 3: Differences mEVP-JFNK with $\alpha = \beta = 300$ (panels (a), (b), (e), (f)) and aEVP-JFNK (panels (c), (d), (g), (h)) using $N_{\mathrm{EVP}} = 50$ (panels (a) – (d)) and $N_{\mathrm{EVP}} = 200$ (panels (e) – (h)) for March 1997 of the ice thickness (in cm) in monthly mean (left column) and the Δ field (in s^{-1}) on the last time level in March 1997 (right column).

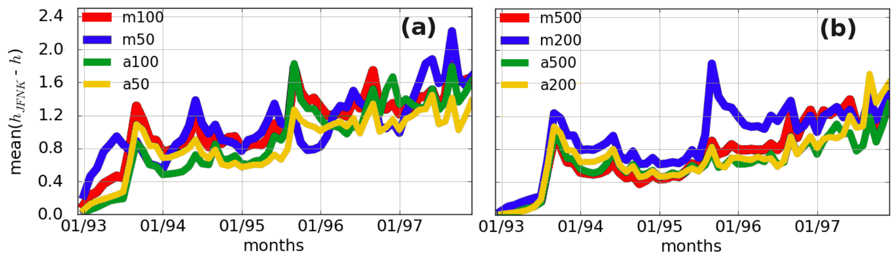

Figure 4: Mean absolute deviations in the ice thickness field (in cm) of the aEVP scheme and the mEVP scheme using $\alpha = \beta = 300$ for $N_{\mathrm{EVP}} = 50$ and 100 (panel (a)) and or $N_{\mathrm{EVP}} = 200$ and 500 (panel (b)) from the reference solution.

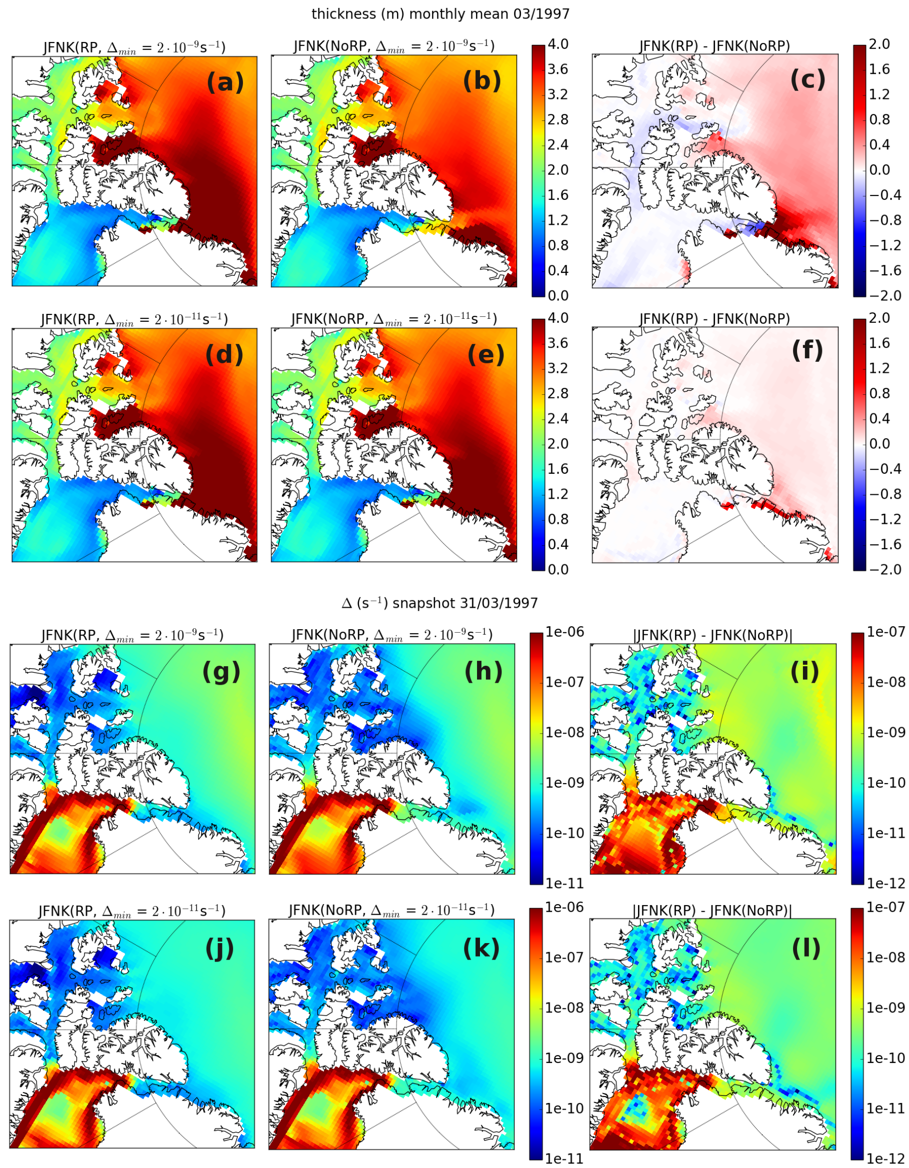

Figure 5: The plots in this figure focus on the Northern CAA and the Lincoln Sea. Graphs (a) – (f) show mean values of ice thicknesses (in m) in March 1997, panels (g) – (l) snapshots of the Δ fields (in s^{-1}) at the end of March 1997. The left column show RP solutions, the center column NoRP solutions, and the right column the differences between them. The panels (a) – (c) and (g) – (i) belong to computations with $\Delta_{\min} = 2 \cdot 10^{-9}\,\mathrm{s}^{-1}$, panels (d) – (f) and (j) – (l) to those with $\Delta_{\min} = 2 \cdot 10^{-11}\mathrm{s}^{-1}$. The maximum thicknesses for RP are 12 m (for $\Delta_{\min} = 2 \cdot 10^{-9} s^{-1}$) and 12.2 m (for $\Delta_{\min} = 2 \cdot 10^{-11}\,\mathrm{s}^{-1}$). For NoRP, the corresponding values are 8 m and 10.5 m. Land shading is omitted in favor of a better visibility of the discretized solutions in the straits.

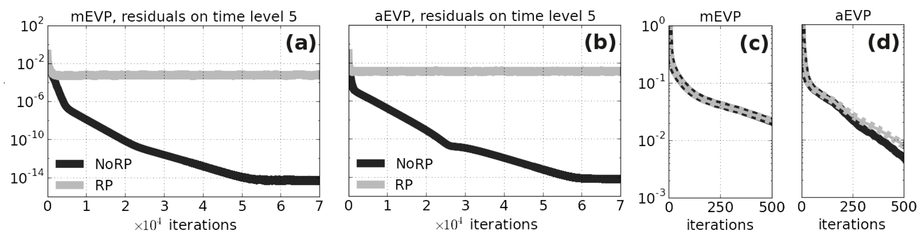

Figure 6: The residuals of the momentum equation (in $\mathrm{m\,s^{-1}}$) with $\Delta_{\min} = 2 \cdot 10^{-9}\,\mathrm{s}^{-1}$ of the aEVP scheme (a) and the mEVP scheme (b) on time level 5 with RP (gray line) and NoRP (black line). The panels (c) and (d) zoom into the first 500 sub-cycling steps of the plots (a) and (b), respectively. The mEVP scheme uses $\alpha = \beta = 300$.

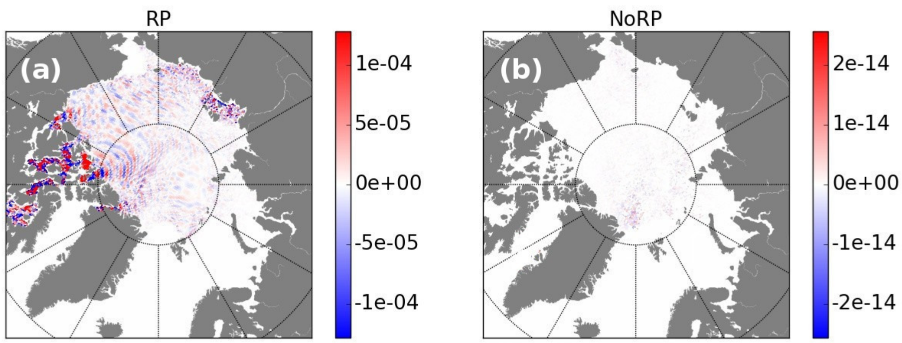

Figure 7: Residuals of the u-equation (in $\mathrm{m\,s^{-1}}$) at the end of time level 5, using the aEVP scheme with 200000 sub-cycling steps and $\Delta_{\min} = 2 \cdot 10^{-9}\,\mathrm{s}^{-1}$ for RP (panel (a)) and NoRP (panel (b)).

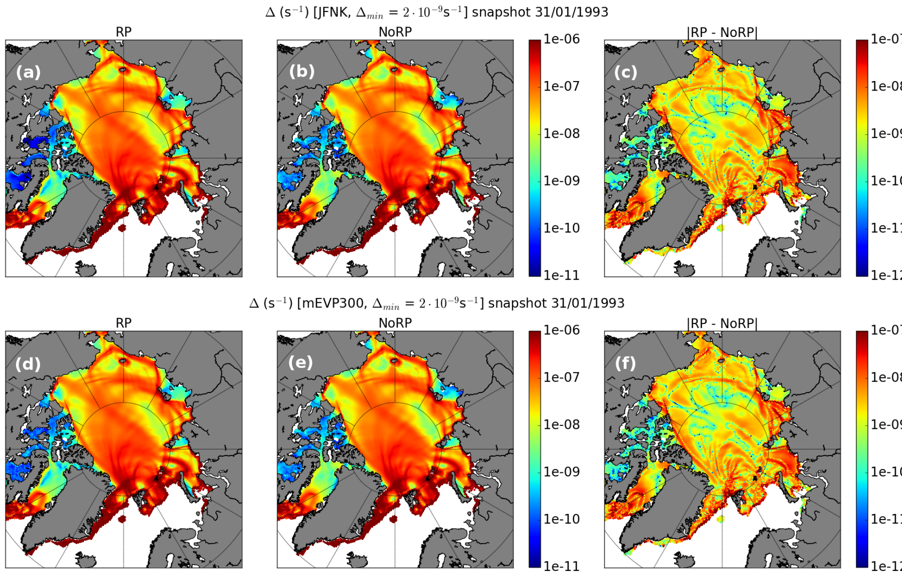

Figure 8: Snapshots of the Δ field (in s^{-1}) on the last time level of January 1993 using $\Delta_{\min} = 2 \cdot 10^{-9}\,\mathrm{s}^{-1}$, RP (left) and NoRP (center) and their absolute differences (right) for the JFNK scheme (panels (a) – (c)) and the mEVP scheme using $\alpha = \beta = 300$, $N_{\mathrm{EVP}} = 500$ (panels (d) – (f)).